Amplitude Modulated Optical Range Data Analysis in Mobile Robotics

Martin D.Adams
Swiss Federal Institute of Technology
Zürich
Switzerland

Abstract

In this paper we consider a time of flight range finder which greatly reduces the correspondence and disparity problems associated with stereo ranging techniques. We present a model for an optical range finder which is capable of detecting untrustworthy range data which results when the optical beam is split between objects of differing range and/or surface reflectivity. We demonstrate a detection scheme for such untrustworthy data using real optical range data.

1 Introduction

In the field of mobile robotics, range sensing is a crucial component of any autonomous system. Mobile robot navigation using simple planar depth maps produced from ranging sensors is still in its infancy. Manipulating the range data robustly, in the presence of range uncertainty is still a problem, even with simple sensors, as will be demonstrated in this section.

The type of sensor considered in this paper is a time of flight range finder which greatly reduces the correspondence and disparity problems associated with stereo ranging techniques [5]. This is achieved by keeping the transmitted and received beams coaxial. This type of sensor consists of a transmitter which illuminates a target with a collimated beam, and a receiver capable of detecting the component of light which is essentially coaxial with the transmitted beam. Often referred to as *optical radars* or *lidars* (*light detection and ranging*), these devices produce a range estimate from the time needed for the light to reach the target and return. A mechanical mechanism sweeps the light beam to cover the required scene.

For close range applications, a simple means of determining the time of flight of the light is by measuring the phase shift between an *amplitude modulated continuous wave* (A.M.C.W.) and its received reflection. This is the technique used in the sensor described in this paper.

An analysis of the sources and propagation of noise within an A.M.C.W. lidar is given in [1], where a noise model is derived so that each sensed range estimate is accompanied by a range variance estimate.

In section 2.1 we note a defect of the A.M.C.W. ranging technique, caused by sudden changes in range and/or surface reflectance. Whilst this effect has been observed in previous literature [2, 3], no solution to this problem has yet been offered. The results in this section demonstrate that even in an optical sensor, the finite width of the light beam can be a significant problem and can result in data points which misrepresent the environment.

In section 3 we consider, in detail, the effect of splitting the light beam between surfaces of differing ranges. Section 3.1 offers a discontinuity detector capable of detecting sudden changes in surface reflectance and range in order to identify 'spurious' data points.

The particular sensor used was developed at A.T&T. Bell Laboratories, U.S.A. Section 4 demonstrates the discontinuity detector using data from the sensor.

2 Lidar Information Maps

Figure 1 shows 720 range data samples taken in a laboratory environment with respect to the centre of the mobile robot (shown as a triangle). The right hand plot shows the same scan result except that it also shows lines, centred on the corrected range observations, of length $2\sigma_r$ (ie: twice the standard deviation associated with the returned signal strength from the sensor model described in [1]) in order to show the uncertainty.

2.1 Sensor Defects

Close examination of figure 1 shows that spurious data points sometimes result immediately before or after detected edges and surface reflectance changes. Between regions D and F in figure 1 for example, the actual range suddenly jumps from 1.26 metres (corresponding to the edge at D on surface AD) to 2.50 metres (the first detected range on surface FG, the maximum range in
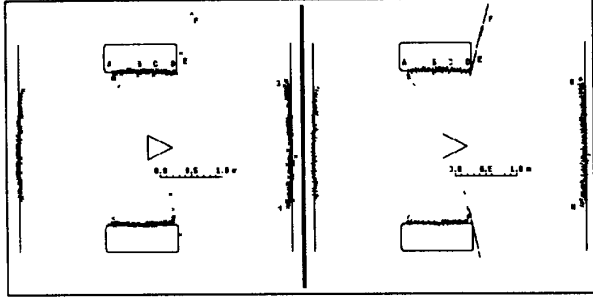
Figure 1: *The left hand plot shows data produced by the lidar in a laboratory environment. In the right hand scan, lines are centred on the range observations having lengths equal to twice the standard deviation associated with the returned signal strength.*

this case). The observed range, according to the sensor, changes from 1.26 metres to only 1.61 metres (point E in figure 1).

Figure 2 shows the reconstructed range and signal strength estimates, as sampled approximately every degree from the output voltages within the vicinity of the edge at D. Close examination of the variation of the ana-
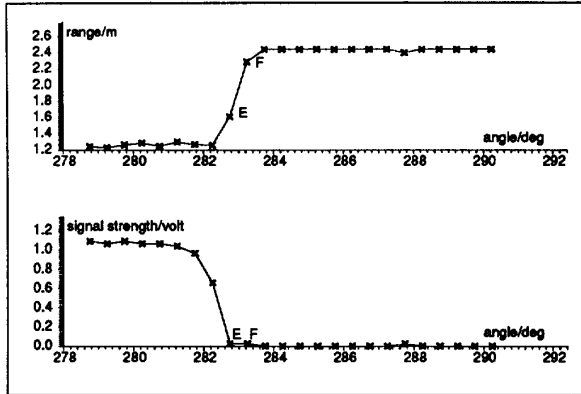

Figure 2: *Graphs showing range and signal strength versus beam angle in the vicinity of the edge marked D in figure 1. Note that single samples only are taken approximately every degree of sensor rotation. Samples E and F were taken as the range voltage was changing.*

logue range voltage with angle shows that by taking only single samples, after the required angular increment, it is easily possible to sample the voltage whilst it is changing. This is the effect which caused the spurious points in figure 1 and the points E and F are shown in figure 2 also.

3 Simultaneous Reflection of Signals from Two Targets

In order to identify spurious data points, the effects of simultaneous reflection from two targets warrants further investigation. The paper by Hebert and Krotkov states that this problem is inherent to A.M.C.W. lidars [2]. To devise a detection scheme for such points, we will analyse the physics involved when an infrared beam is split between two targets.

Consider a transmitted reference signal $V_0 \cos \omega t$ which is incident upon an edge (figure 3). An area A_1 is
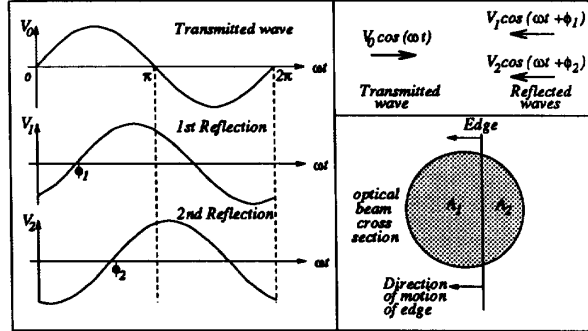

Figure 3: *The transmitted signal is split into two returned signals of differing phase by an edge. As the beam traverses the edge the illuminated areas and hence returned signal amplitudes will vary with traversal time.*

illuminated on the closer of the two surfaces returning a signal $V_1 \cos(\omega t + \phi_1)$, whilst an area A_2 is illuminated on the further surface yielding a signal $V_2 \cos(\omega t + \phi_2)$. The signal returned to the sensor will actually be the result of many modulated signals $\sum_{i=1}^{n} V_i \cos(\omega t + \phi_i)$, each being emitted from a small area δA_i within the infrared beam cross section. For a small beam cross sectional area the analysis is simplified if we assume that during the time the beam traverses the edge, ϕ_1 and ϕ_2 remain constant and that V_1 and V_2 change only due to changes in A_1 and A_2. Changes in ϕ as the beam moves across areas A_1 or A_2 individually are therefore assumed to be negligible. Hence the returned signal Y is given by:

$$Y = V_1 \cos(\omega t + \phi_1) + V_2 \cos(\omega t + \phi_2) \qquad (1)$$

which can be written as a single sinusoid:

$$Y = V \cos \phi \cos \omega t - V \sin \phi \sin \omega t = V \cos(\omega t + \phi) \qquad (2)$$

which is the form that is estimated at the sensor outputs - ie: V is the output signal strength produced by both targets and ϕ the resulting phase shift.

From equations 1 and 2 we see that:

$$\cos \phi = \frac{V_1}{V} \cos \phi_1 + \frac{V_2}{V} \cos \phi_2 \qquad (3)$$

9

and:

$$\sin \phi = \frac{V_1}{V} \sin \phi_1 + \frac{V_2}{V} \sin \phi_2 \qquad (4)$$

giving two simultaneous equations in V and ϕ. Eliminating ϕ gives:

$$V^2 = V_1^2 + 2V_1V_2 \cos(\phi_1 - \phi_2) + V_2^2 \qquad (5)$$

Before we can proceed further we need to determine, as generally as possible, the relationship between each returned voltage, the sensor to target range and the illuminated area. We make the assumption that the emitted power is uniformly spread over the cross sectional area of the beam. Therefore:

$$V_{1,2} = K_{1,2} \frac{A_{1,2}}{F(R_{1,2})} \qquad (6)$$

where the subscripts 1 and 2 refer the reflected signals 1 and 2, $K_{1,2}$ are constants for each surface and incorporate surface reflectances and beam to target angles of incidence, and $F(R_{1,2})$ represents a function of the sensor to target ranges $R_{1,2}$.

To establish a relationship between K_1 and K_2 in equations 6, we consider the magnitude of the returned signal strengths when each surface is illuminated *independently*. We denote these as V_{e1} and V_{e2} We will call these the *end* conditions and in general:

$$V_{e2} = \eta V_{e1}, \quad \frac{K_1}{K_2} = \frac{V_{e1}F(R_1)}{V_{e2}F(R_2)} \qquad (7)$$

Hence by substitution of equations 6 and 7 into equation 5 we get:

$$V^2 = \frac{K_1^2}{[F(R_1)]^2}[A_1^2 + 2\eta A_1 A_2 \cos(\phi_1 - \phi_2) + \eta^2 A_2^2] \quad (8)$$

Equation 8 gives V, the returned signal amplitude, as a function of the beam cross sectional area illuminating each end condition. Substitution of this function along with equations 6 and 7 into either of equations 3 or 4 gives the phase shift estimate ϕ as a function of time, as the beam crosses the edge.

The above theory can be used for the detection of range readings such as points E and F in figure 1. We will show in the following section that the motion of the infrared beam across an edge is only a particular case to which the above theory can be applied. The estimated phase and amplitude of any single reading can be considered to be the result of the addition of two signals from any two arbitrary 'end' conditions, which do not have to lie either side of an edge. By generalising this theory to any range and amplitude estimate, we will derive a method for the detection of spurious data such as points E and F in figure 1.

3.1 Discontinuity Detection

Before proceeding, we make a distinction between what we will refer to as a *discontinuity* and an *edge*. We will use the term discontinuity to refer to an abrupt change in the signal amplitude. We label an edge as an abrupt change in the sensor to target range, as we human beings would perceive a true edge. Note that a discontinuity can be the result of an edge *or* a change in surface reflectance, as the sensor head rotates.

We also now clarify the constraints upon our end conditions. Equation 8 is only valid if the sum of the components of the areas normal to the optical beam, which illuminates each end point is constant, ie:

$$A_1 + A_2 = A \qquad (9)$$

where A is the cross sectional area of the beam. This means that the chosen end conditions must be spatially joined in the plane of the scanning infrared beam. This is shown in figure 4. We assume that there is a verti-
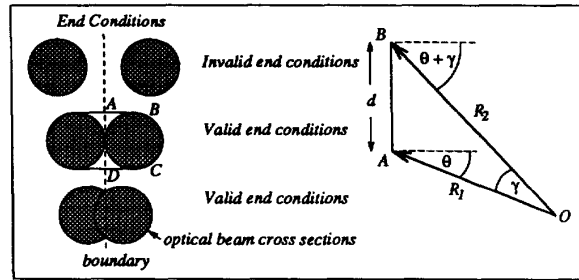

Figure 4: *The relationship between chosen end conditions.*

cal boundary across which there is a possible change in range or surface reflectance. Due to the small optical beam diameter (2 cm in our case), we make the approximation that an 'end condition' is not just restricted to the circular beam cross section, but occupies the arched region marked ABCD in figure 4. This means that equation 9 is valid in equation 8. Within the arched region ABCD, the *actual* values of R_1 and K_1 can change, but the *sensed* values of R_1 and K_1 will remain constant.

Eliminating A_2 in equation 8, from equation 9, and differentiating V^2 with respect to variable A_1 shows that there is always a position between the end points at which V is stationary with respect to A_1. The second derivative of the square of the signal amplitude with respect to A_1 is given by:

$$\frac{\partial^2 (V^2)}{\partial A_1^2} = \frac{2K_1^2}{F(R_1)^2}[1 + \eta^2 - 2\eta \cos(\phi_1 - \phi_2)] \qquad (10)$$

which is independent of A_1. $\frac{\partial^2(V^2)}{\partial A_1^2}$ is therefore constant as the beam traverses from one end condition to the

10

other, the value of this constant being dependent upon the end conditions only, ie: ϕ_1, ϕ_2, η and K_1. From equation 10 we can find the nature of the stationary value of V^2 versus A_1. Simple analysis shows that for all values of ϕ_1, ϕ_2 and η, $\frac{\partial^2(V^2)}{\partial A_1^2}$ is always positive (meaning that V^2 has a minimum with respect to A_1) and approaches zero as $\eta \to 1$ and $\phi_1 \to \phi_2$, ie: if the end conditions are similar, $\frac{\partial^2(V^2)}{\partial A_1^2} \to 0$. This is demonstrated by the experimental results shown in figure 5 where V is plotted against time. We can therefore conclude that
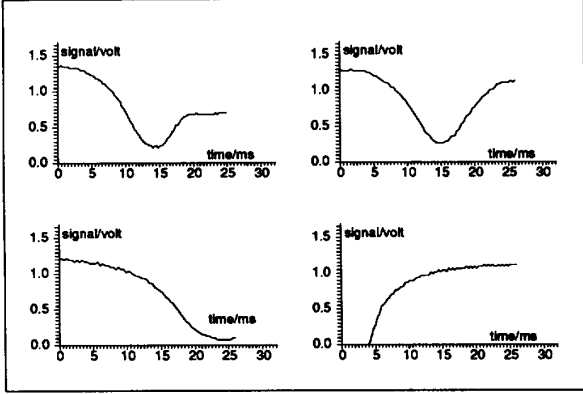

Figure 5: *Graphs of signal amplitude versus time as the infrared beam traverses different end conditions.*

the numerical value of $\frac{\partial^2(V^2)}{\partial A_1^2}$ across two end conditions gives us an indication of how 'different', in terms of either sensor to target range and/or surface reflectance, the end conditions are. $\frac{\partial^2(V^2)}{\partial A_1^2}$ will rarely actually be zero in practice since two end conditions will rarely be identical even when the beam does not pass a discontinuity. It therefore remains for us to determine a value for $\frac{\partial^2(V^2)}{\partial A_1^2}$, beyond which we assume a discontinuity has been passed possibly resulting in spurious data such as E and F in figure 1.

We also need to note that the reflected infrared light from a target contains two components, one being a specular component which follows Fresnel's equations and the other a diffuse component which is approximately described by Lambert's cosine law [4]. Because of the coaxial design of the sensor, specular reflections can only be received at very near normal incidence and in practice are only noticed with extremely reflective targets. Therefore, except for these rather rare cases, only the diffuse component need be considered.

We now consider in more detail the value of $\frac{\partial^2(V^2)}{\partial A_1^2}$ when the beam traverses a discontinuity. Consider the right hand diagram in figure 4. R_1 and R_2 are two successive range estimates which we will choose as arbitrary end conditions. According to Lambert's cosine law, the

amplitude of the returned signal in each case is given by:

$$V_{e1} = \frac{\rho_1 A \cos\theta}{R_1^2}, \quad V_{e2} = \frac{\rho_2 A \cos(\theta + \gamma)}{R_2^2} \quad (11)$$

where $\rho_{1,2}$ are the surface reflectance constants from points A and B and γ is the angle between resulting data points. In general, between end points A and B in figure 4, $\rho_1 \neq \rho_2$. Hence, from the figure:

$$\eta = \frac{V_{e2}}{V_{e1}} = \frac{\rho_2 R_1^2 \cos(\theta + \gamma)}{\rho_1 R_2^2 \cos\theta} = \frac{\rho_2}{\rho_1}\left(\frac{R_1}{R_2}\right)^3 \quad (12)$$

Applying the sine rule to triangle OAB in figure 4 and from equations 11 and 12 we define $S = \frac{\partial^2(V^2)}{\partial A_1^2}$ as:

$$S = 2\rho_1^2 \frac{R_2^2 \sin^2\gamma}{d^2 R_1^4}[1 + \left(\frac{\rho_2}{\rho_1}\right)^2\left(\frac{R_1}{R_2}\right)^6$$

$$-2\left(\frac{\rho_2}{\rho_1}\right)\left(\frac{R_1}{R_2}\right)^3 \cos[K(R_1 - R_2)]] \quad (13)$$

where K is a constant relating phase shift to actual range and R_1 and R_2 are related by the cosine rule:

$$d^2 = R_1^2 + R_2^2 - 2R_1R_2\cos\gamma \quad (14)$$

Between equations 13 and 14, it is possible to eliminate d and determine a relationship between S, R_1, R_2, ρ_1 and ρ_2.

It is possible to determine numerical solutions to equation 13 so that threshold values for S can be determined as a function of R_1, the first detected range. When this adaptive threshold is exceeded, equation 13 indicates a range discontinuity at constant surface reflectivity ie: when $\rho_1 = \rho_2$. Numerical solutions to equation 13 also show that changes in surface reflectivity between end conditions, at constant range, can be detected under the same adaptive threshold value for S. An in depth analysis into the range/reflectance sensitivity of S is given in [1]. As a result of this analysis we have built a detector which has a high success rate at identifying such points when they are caused by *either* range *or* reflectance changes. When both effects occur simultaneously we have quantified the interaction which, under certain circumstances, can result in no discontinuity detection.

4 Results

Figure 6 shows a high density scan (left hand plot) and processed scan (right hand plot). The left hand scan shows a dense 360° plot of the environment, each sample taken at a time interval of 0.1 milliseconds. Between points J and K on the lower pillar, a coloured target was positioned causing a change in surface reflectivity. The effects of the discontinuity can be seen at J and K, and also at the pillar edges.
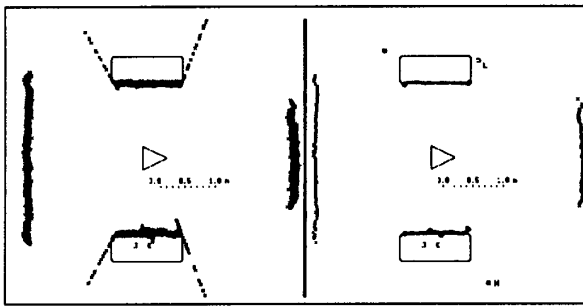
11

Figure 6: *Discontinuity detection using 13474 samples from a single scan. In the right hand scan detected discontinuities are plotted as circles, and points with zero returned signal amplitude are shown as squares.*

In this first scan we used all eight bits of the analogue to digital converter to convert ranges up to 2.5 metres only. The scan is made up of 13474 samples, and every 18 of these were used to form a single data point on the right hand range map. Along with each new data point, a value for S was established and compared with S_{th}, the adaptive threshold value of S.

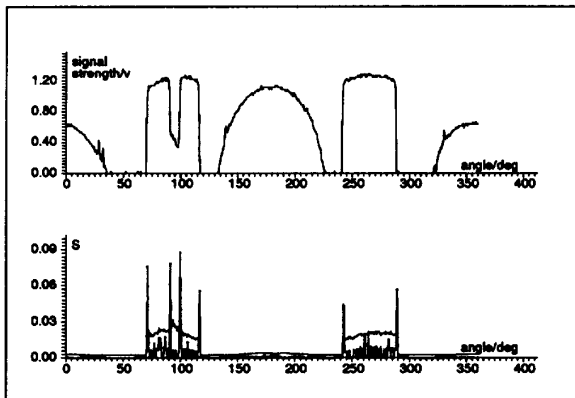In figure 7 the top curve shows the variation of signal strength with angle, during the scan of figure 6. Notice

Figure 7: *Signal amplitude (top graph) and S (bottom graph) versus scan angle as computed experimentally during the previous scan. S_{th} is superimposed upon the data in the lower graph.*

the dip at an angle of approximately 85°, due to the darker region JK in figure 6. The lower graph shows the estimated value of S for each data point in the right hand plot of the scan. The large spikes occur at both range and reflectance discontinuities. Superimposed upon this plot is a curve of S_{th}, the adaptive threshold value for S, versus sensor angle. Notice how S_{th} adapts to the changes in range at angles of approximately 70°, 115°, 240° and 290°. Only the spikes produced in the estimation of

S rise above S_{th}. These points are plotted as circles in the right hand scan of figure 6, see for example point L in the figure.

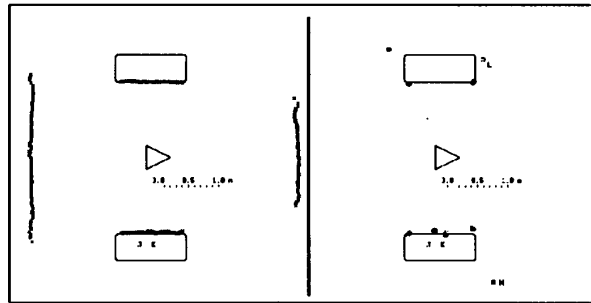We now have enough information from the sensor to be able to produce the scans shown in figure 8. The

Figure 8: *Range data which has successfully passed through the discontinuity detector (left scan) and data which has failed the test (right scan).*

left hand scan shows 'filtered' or trustworthy data. Each data point in this scan has passed through the discontinuity detector successfully, and has an associated range variance estimate (see [1]). The right hand plot shows the points which failed the discontinuity test. Point M (shown as a square in both figures 6 and 8) has occurred as a result of the sensor estimating that all 18 data samples from the left hand scan of figure 6, have a signal amplitude of 0 volts. This is an example of an undesirable feature of the particular sensor used, namely its inability to always estimate a finite signal amplitude, when the actual signal amplitude falls below a certain value. Because of this, S cannot be estimated and we cannot place any confidence in this data point.

Hence, within the working capabilities of our discontinuity detector (outlined in section 3), we are confident that all of the range data shown in the left hand scan of figure 8 is 'true' data. Notice also the much improved variance in the range data of the right hand scan of figure 6 to that in the left scan, due to the averaging of 18 samples per data point.

Figure 9 shows an uncorrected scan (left hand plot) and a phase corrected scan (right hand plot) after calibration. The number of samples recorded was reduced to 5600.

Notice that the sensor is sensitive enough to resolve the small changes in the range data in figure 9, caused by thin vertical pipes on the wall at A and B. The graphs in figure 10 show the variation of S_{th} and S versus sensor azimuth, as the scan was recorded. Notice again that the detector adapts its thresholding technique to the environment surrounding the sensor, [1]. Figure 11 shows the results of using the thresholding technique on the calibrated data from figure 9. The left hand scan shows
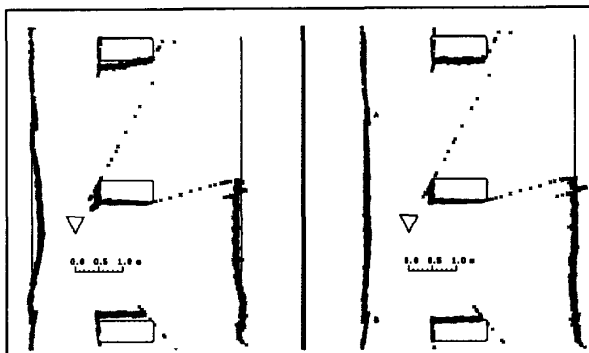
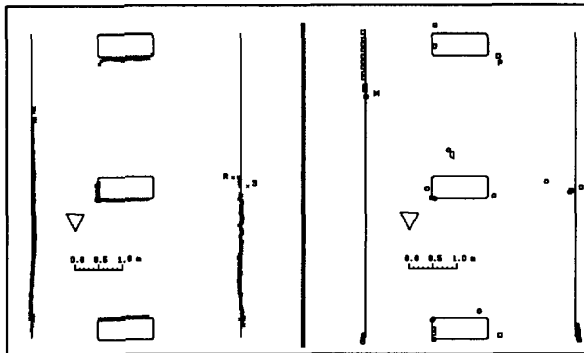Figure 9: *Uncorrected and corrected range scans using 5600 data samples.*

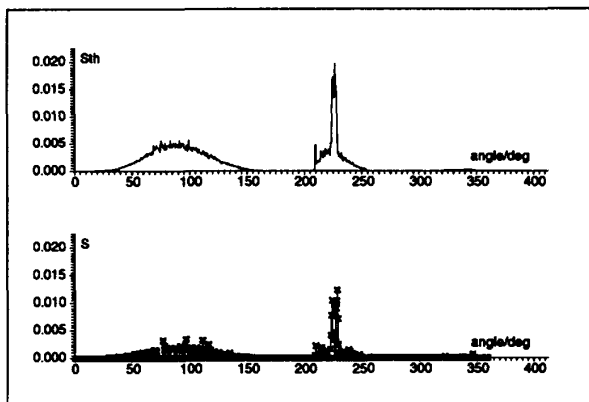Figure 11: *Accepted and rejected data, after filtering with the detector*

Figure 10: S_{th} *(top graph) and S (bottom graph) versus sensor azimuth for the calibrated scan in the previous figure.*

data which has successfully passed through the detector. The right hand scan shows the data which either carried no returned signal strength (plotted as squares) or failed the discontinuity test (plotted as circles).

Points P and Q in figure 11 show data resulting from a split optical beam at the edge of the pillar close to the mobile. At point P, not enough of the pillar is illuminated to give any signal amplitude estimate. The discontinuity detector cannot operate here and therefore a square is plotted at P. At Q however, enough of the optical beam illuminates the pillar so that the net signal amplitude with each of the four points used to create point Q can be used to estimate S. Q has been captured by the discontinuity detector.

5 Summary

In this paper we have considered in detail the effect of splitting the light beam between two targets. In previous

work the cause of the spurious points has not received much attention, and it has simply been stated that they are inherent in any A.M.C.W. optical system and cannot be removed [2].

In response to this we have built a detector which has a high success rate at identifying such points when they are caused by *either* reflectance *or* range changes. When both effects occur simultaneously, we have quantified the interaction which, under certain circumstances, can result in no detection. The detector is not fool proof, but has been shown to operate successfully in our results, in many different indoor environments.

6 Acknowledgements

References

[1] M. D. Adams. *Optical Range Data Analysis for Stable Target Pursuit in Mobile Robotics.* PhD thesis, University of Oxford, U.K., 1992.

[2] Martial Hebert and Eric Krotkov. 3-D Measurements From Imaging Laser Radars: How Good Are They? In *International Conference on Intelligent Robots and Systems*, pages 359–364, 1991.

[3] Ralf Hinkel and Michael Weidmann. First Results in Real Time Position Estimation with a Laser Radar. Technical report, Computer Science Department, University of Kaiserslautern, Germany, 1989.

[4] P. Moon. *The Scientific Basis of Illuminating Engineering.* Dover Publications, New York, U.S.A., 1961.

[5] David Nitzan, Alfred E. Brain, and Richard O. Duda. The Measurement and Use of Registered Reflectance Data in Scene Analysis. In *Proceedings of the I.E.E.E.*, pages 206–220, 1977.